Journal of Science and Technology – Engineering and Technology for Sustainable Development
Volume 36, Issue 4, October 2026, 001–009

Multi-Fidelity Analysis of a Composite Beam

***Nguyen Xuan Thuc*[1], *Nguyen Anh Tuan*[2], *Nguyen Van Huy*[2,*],**
***Nguyen Hai Nam*[2], *Duong Van Quang*[2],**
[1]Viettel High Technology Industry Corporation - Viettel Group, Ha Noi, Vietnam
[2]Le Quy Don Technical University, Ha Noi, Vietnam
[*]Corresponding author email: nguyenvanhuy@lqdtu.edu.vn

Abstract

Composite materials are widely used in engineering because they are light, strong, and resistant to corrosion. However, their complex structure makes it difficult to predict their mechanical behavior. This paper presents a simple and effective method for analyzing a composite cantilever beam. The analysis is performed at multiple levels, starting from the small-scale properties of the fiber and matrix materials. First, the material properties of a single composite ply are calculated using micromechanics and semi-empirical formulas. These properties include stiffness, strength, and Poisson's ratio. Then, the Classical Lamination Theory (CLT) is applied to determine the overall properties of the composite laminate, which consists of many plies stacked together. An improved Tsai-Wu failure criterion is used to evaluate the strength of the laminate. Finally, the Euler-Bernoulli beam theory is employed to calculate the mechanical responses of the beam, such as displacement, stress, and inverse safety factor under different loading conditions. The calculated results are compared with finite element simulations using ANSYS. The comparison shows good agreement between the two methods, with small differences in most cases. The proposed method suggests a new approach for UAV structural analysis by modeling slender UAV components as equivalent beams. This approach enables fast and efficient structural evaluation, making it well suited for the preliminary design stage of UAV development.

Keywords: Composite beam, composite ply, classical lamination theory, laminate, strength.

1. Introduction

Composite materials are being applied in various industrial fields thanks to their outstanding properties such as lightweight, high strength, and excellent corrosion resistance [1, 2]. However, to ensure their effective utilization, accurately determining their material properties and conducting structural analysis play a crucial role.

Material properties, including Young modulus, Poisson's ratio and strength are fundamental to the design of composite structures. However, due to their heterogeneous and anisotropic properties, calculating these properties is more challenging than for traditional isotropic materials. Composite material properties depend on factors such as fiber volume ratio, fiber orientation, and layering order [1].

In previous studies, many methods have been developed to calculate the material properties of composites such as experiments, finite element method (FEM). However, each method has certain limitations: experiments are often time-consuming and costly, while the FEM method requires large resources and computational time [1, 3-5].

Machine learning is also emerging as an effective method for calculating composite material parameters. Zang *et al.* [6] combined finite element analysis (FEA) and machine learning to predict material parameters of composite panels. Sun *et al.* [7] proposed a method using convolutional neural networks (CNN) to predict stress fields in fiber-reinforced composite materials.

In this paper, we present a multi-scale analysis of a composite beam, starting from the evaluation of ply-level properties to the prediction of the beam's mechanical response. The properties of the composite ply are determined using micromechanics and semi-empirical models based on the constituent fiber and matrix materials. Laminate-level properties are then derived from ply properties using Classical Laminate Theory (CLT) and an improved Tsai-Wu failure criterion. Finally, the mechanical behavior of the composite beam is analyzed using the Euler-Bernoulli beam theory. These results provide the foundation for developing an algorithm used in the preliminary design stage of composite components. This algorithm allows fast calculation of displacements, strains, and stresses for multiple design alternatives derived from different material combinations.

p-ISSN 3093-3242
e-ISSN 3093-3579
https://doi.org/10.51316/jst.193.etsd.2026.36.4.x
Received: Dec 7, 2025; Revised: Feb 4, 2026;
Accepted: Feb 27, 2026; Online: Jul 16, 2026

2. Methodology

2.1. Properties of Unidirectional Ply

Unidirectional ply is a ply with fibers distributed parallel in a certain direction. The material properties of unidirectional layers can be calculated by several methods such as: micromechanics, semi-empirical method, FEM, ... In these methods, the micromechanics method is a simple method suitable for calculating properties such as Young's modulus, Poisson's ratio in the longitudinal direction because these properties less effect by the distribution of fibers, stress and strain [1].

$$E_1 = E_{f1}\upsilon_f + E_m\upsilon_m$$
$$\nu_{12} = \nu_{f12}\upsilon_f + \nu_m\upsilon_m \tag{1}$$

where υ_f, υ_m are volume ratio of fiber and matrix, respectively.

The transverse modulus E_2 and shear modulus G_{12} are calculated using a semi-empirical method based on Halpin-Tsai equations [8]:

$$E_2 = \frac{E_m\left(1+\xi\eta\upsilon_f\right)}{1-\eta\upsilon_f},\ \eta = \frac{E_{f2}-E_m}{E_{f2}+\xi E_m}$$
$$G_{12} = G_m\frac{1+\xi\eta\upsilon_f}{1-\eta\upsilon_f},\ \eta = \frac{G_{f12}-G_m}{G_{f12}+\xi G_m} \tag{2}$$

where ξ is a fitting parameter; typically, $\xi = 1$ for glass and carbon fiber, while $\xi = 2$ for boron fiber [8].

Poisson's ratio ν_{23} is determined by equation [9]:

$$\nu_{23} = 1 - \frac{\nu_{12}E_2}{E_1} - \frac{E_2}{2K} + \frac{E_2\left(1-2\nu_{12}\right)}{2E_1} \tag{3}$$

Shear modulus G_{23} is calculated as follows [10]:

$$G_{23} = \frac{G_m\left[K_m\left(G_m+G_{f23}\right)+2G_{f23}G_m+K_m\left(G_{f23}-G_m\right)\upsilon_f\right]}{K_m\left(G_m+G_{f23}\right)+2G_{f23}G_m-\left(K_m+2G_m\right)\left(G_{f23}-G_m\right)\upsilon_f} \tag{4}$$

If the fiber failure strain $e_{f1}^{(+)}$ is smaller than the matrix failure strain $e_{m1}^{(+)}$, the longitudinal tensile strength is:

$$s_L^{(+)} = e_{f1}^{(+)}E_{1c} \tag{5}$$

If the fiber failure strain $e_{f1}^{(+)}$ is greater than the matrix failure strain $e_{m1}^{(+)}$, the longitudinal tensile strength is:

$$s_L^{(+)} = e_{m1}^{(+)}E_{c1} = \frac{s_{m1}^{(+)}}{E_{m1}}E_{c1} \tag{6}$$

The longitudinal compressive strength is difficult to determine, as composite materials under compressive loading may fail through various mechanisms, such as "out-of-plane" and "in-plane" failure modes. In addition, the compressive strength is strongly influenced by the initial fiber misalignment. Although the misalignment angle may be very small (on the order of a few degrees), it can significantly reduce the compressive strength [10].

In the case of "out-of-plane" mode, the longitudinal compressive strength is given by [10]:

$$s_L^{(-)} = 2\upsilon_f\left[\frac{E_mE_f\upsilon_f}{3\left(1-\upsilon_f\right)}\right]^{1/2} \tag{7}$$

while in the case of "in-plane" mode [10]:

$$s_L^{(-)} = \frac{G_m}{1-\upsilon_f} \tag{8}$$

When the initial fiber misalignment φ is taken into account, the longitudinal compressive strength is [10]:

$$s_L^{(-)} = \frac{s_{mLT}}{\varphi + \dfrac{s_{mLT}\left(1-\upsilon_f\right)}{G_m}} \tag{9}$$

The longitudinal compressive strength is the minimum of the three values calculated from , and .

The transverse tensile strength of a unidirectional composite $s_T^{(+)}$ is low due to stress concentrations around the fibers.

$$s_T^{(+)} = \frac{E_2s_m^{(+)}}{E_mF} \tag{10}$$

where F is strain concentration factor $\left(F>1\right)$, which depends on fiber diameter and spacing [1].

Similarly, transverse compressive strength $s_T^{(-)}$ and shear strength s_{LT} are determined as follows:

$$s_T^{(-)} = \frac{E_2s_m^{(-)}}{E_mF},\qquad s_{LT} = \frac{G_{12c}s_{LTm}}{G_mF_s} \tag{11}$$

where F_s is the in-plane shear strain concentration factor [1].

2.2. Properties of Composite Laminate

Composite laminates consist of multiple plies oriented in the desire directions and bonded together. Properties of laminates are determined based on Classical Lamination Theory [1].

$\mathbf{S},\mathbf{Q}$ are the stiffness and compliance matrices of the unidirectional plies in the principal coordinate system O123. Using transformation matrix, the stiffness and compliance matrices $\bar{\mathbf{S}},\bar{\mathbf{Q}}$ in the off-axis coordinates *Oxyz* are calculated as follows:

$$\bar{\mathbf{S}} = \mathbf{T}_{\varepsilon}^{-1}\mathbf{S}\mathbf{T}_{\sigma}; \qquad \bar{\mathbf{Q}} = \left[\bar{\mathbf{S}}\right]^{-1} \tag{12}$$

$$\mathbf{S} = \begin{bmatrix} 1/E_1 & -\nu_{12}/E_1 & -\nu_{12}/E_1 & 0 & 0 & 0 \\ -\nu_{12}/E_1 & 1/E_2 & -\nu_{23}/E_2 & 0 & 0 & 0 \\ -\nu_{12}/E_1 & -\nu_{23}/E_2 & 1/E_2 & 0 & 0 & 0 \\ 0 & 0 & 0 & 1/G_{23} & 0 & 0 \\ 0 & 0 & 0 & 0 & 1/G_{12} & 0 \\ 0 & 0 & 0 & 0 & 0 & 1/G_{12} \end{bmatrix} \tag{13}$$

$$\mathbf{T}_{\varepsilon} = \begin{bmatrix} c^2 & s^2 & 0 & 0 & 0 & cs \\ s^2 & c^2 & 0 & 0 & 0 & -cs \\ 0 & 0 & 1 & 0 & 0 & 0 \\ 0 & 0 & 0 & c & s & 0 \\ 0 & 0 & 0 & -s & c & 0 \\ -2cs & 2cs & 0 & 0 & 0 & c^2-s^2 \end{bmatrix} \tag{14}$$

$$\mathbf{T}_{\sigma} = \begin{bmatrix} c^2 & s^2 & 0 & 0 & 0 & 2cs \\ s^2 & c^2 & 0 & 0 & 0 & -2cs \\ 0 & 0 & 1 & 0 & 0 & 0 \\ 0 & 0 & 0 & c & s & 0 \\ 0 & 0 & 0 & -s & c & 0 \\ -cs & cs & 0 & 0 & 0 & c^2-s^2 \end{bmatrix} \tag{15}$$

where $s = sin(\theta)$, $c = cos(\theta)$, θ is the ply angle.

$\mathbf{N} = \left[N_x, N_y, N_z\right]^T$, $\mathbf{M} = \left[M_x, M_y, M_z\right]^T$ are forces and moments apply to, the strain $\boldsymbol{\varepsilon}$ and curvature $\boldsymbol{\kappa}$ of laminate are:

$$\begin{bmatrix} \mathbf{N} \\ \mathbf{M} \end{bmatrix} = \begin{bmatrix} \mathbf{A} & \mathbf{B} \\ \mathbf{B} & \mathbf{D} \end{bmatrix} \begin{bmatrix} \boldsymbol{\varepsilon} \\ \boldsymbol{\kappa} \end{bmatrix} \tag{16}$$

where the laminate extensional stiffnesses

$$A_{ij} = \int_{-t/2}^{t/2} \left(\bar{Q}_{ij}\right)_k dz = \sum_{k=1}^{N} \left(\bar{Q}_{ij}\right)_k \left(z_k - z_{k-1}\right) \tag{17}$$

the laminate-coupling stiffnesses are given by

$$B_{ij} = \int_{-t/2}^{t/2} \left(\bar{Q}_{ij}\right)_k z dz = \frac{1}{2}\sum_{k=1}^{N} \left(\bar{Q}_{ij}\right)_k \left(z_k^2 - z_{k-1}^2\right) \tag{18}$$

and laminate-bending stiffnesses are given by

$$D_{ij} = \int_{-t/2}^{t/2} \left(\bar{Q}_{ij}\right)_k z^2 dz = \frac{1}{3}\sum_{k=1}^{N} \left(\bar{Q}_{ij}\right)_k \left(z_k^3 - z_{k-1}^3\right) \tag{19}$$

where the subscriptions *i, j = 1, 2, or 6*; $\bar{\mathbf{Q}}_k$ is stiffness matrix of the kth ply in off-axis coordinates.

The inverse of matrix $\mathbf{A}$ yields matrix $\mathbf{A'}$, which is then used to determine the material properties of the laminate [1].

$$\begin{gathered} E_1 = \frac{1}{tA'_{11}};\ E_2 = \frac{1}{tA'_{22}}; \\ G_{12} = \frac{1}{tA'_{66}};\ G_{23} = \frac{1}{tA'_{44}};\ G_{31} = \frac{1}{tA'_{55}}; \\ \nu_{12} = \frac{-A'_{21}}{A'_{11}};\ \nu_{23} = \frac{-A'_{32}}{A'_{22}};\ \nu_{13} = \frac{-A'_{31}}{A'_{11}} \end{gathered} \tag{20}$$

where t is the laminate's thickness.

The strength of the laminate is evaluated using an improved Tsai-Wu failure criterion proposed by Chen *et al.* [11]. In this criterion, the interaction coefficients corresponding to stresses in different directions f_{12}, f_{23} are calculated separately depending on whether the loading is tensile or compressive. The improved criterion yields more accurate results compared to the original Tsai-Wu failure theory.

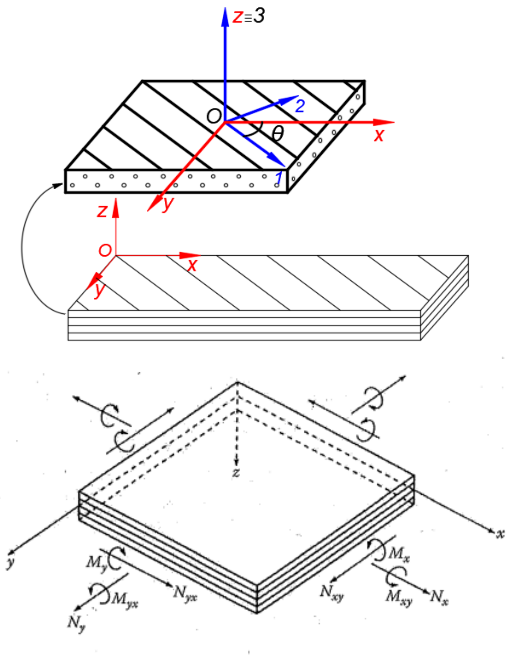

Fig. 1. Coordinate systems, forces and moments acting on laminate

2.3. Theoretical Method to Determine Mechanical Responses of Composite Beams

Beam is structure that have one dimension (length) much larger than the other two (cross-section dimensions). This type of structure is widely used in the aerospace structures. In particular, for Unmanned Aerial Vehicles (UAVs), beams are often made of composite materials. Therefore, the structural analysis of composite beams provides the foundation for more advanced analyses of aerospace structures.

This section presents a method to determine mechanical responses of composite beams. A cantilever beam with a rectangular cross-section shown in Fig. 2a is considered, in which the cap is made of unidirectional composite plies and the web is made of woven composite plies. These two composites are made from AS4 carbon fiber and 3501-6 epoxy resin (Table 2). The core of the beam is made of isotropic material Rohacell (Table 1). Fig. 2b illustrates the two loading cases considered in the analysis. The mechanical responses of this beam include displacement, stresses, and inverse safety factor are evaluated.

The beam is made of parts with different materials, the bending rigidity about the *y*-axis (Fig. 2) of the section is the sum of the bending rigidity of the parts

$$EI = \sum (EI)_i = (EI)_{web} + (EI)_{cap} + (EI)_{core} \tag{21}$$

where $(EI)_{web} = E_{x\_web} I_{web}$, E_{x_web} is effective Young's modulus of the web (a laminate consists of 10 woven plies), calculated using . Similarly, for the isotropic core, $(EI)_{core} = E_{core} I_{core}$. For the cap, bending rigidity is calculated as follows:

$$(EI)_{cap} = \frac{M_x}{\kappa_x} \tag{22}$$

where $\boldsymbol{\kappa} = \left[\kappa_x, \kappa_y, \kappa_z\right]^T$ is the curvature of the beam's neutral axis under bending moment **M**. On the other hand, according to , for a symmetrically stacked laminate (with laminate-coupling stiffness matrix **B**=0), the curvature $\boldsymbol{\kappa}$ is calculated as following:

$$\boldsymbol{\kappa} = \mathbf{D}^{-1}\mathbf{M} \tag{23}$$

From (22) and (23), bending rigidity about the *y*-axis of the cap is defined as the inverse of the (1,1) component of the inverse laminate-bending stiffness matrix:

$$(EI)_{cap} = \frac{1}{\left[\mathbf{D}^{-1}\right]_{11}} \tag{24}$$

where **D** is the laminate-bending stiffness matrix of the laminate computed from CLT.

The displacement of the beam in the z-direction, denoted as $w(x)$, is governed by the Euler–Bernoulli beam equation:

$$M_x(x) = EI\frac{d^2 w(x)}{dx^2} \tag{25}$$

Double integration yields the displacement $w(x)$, while the normal stress is calculated using the following expression:

$$\sigma_x = \frac{M_x(x)}{EI} Ez \tag{26}$$

Since the bending load is primarily carried by the beam caps, while the webs mainly resist shear forces, the cross-section of the beam can be idealized as shown in Fig. 3. Two webs are represented by a continuous panel of thickness t_{web}, while two caps are replaced by two booms with cross-sectional area B_r, positioned symmetrically at the top and bottom of the section. The shear modulus of core is much lower than that of the web, resulting in significantly lower shear stresses in the core compared to those in the web. Therefore, it is reasonable to assume that the shear load is primarily carried by the web, and the core can be neglected in the idealization. This approach is based on the structural idealization theory proposed by Megson [12].

Table 1. Material properties of Rohacell core

E (MPa)	*G* (MPa)	ν	Tensile strength (MPa)	Compressive strength (MPa)
75	24	0.49	1.6	0.8

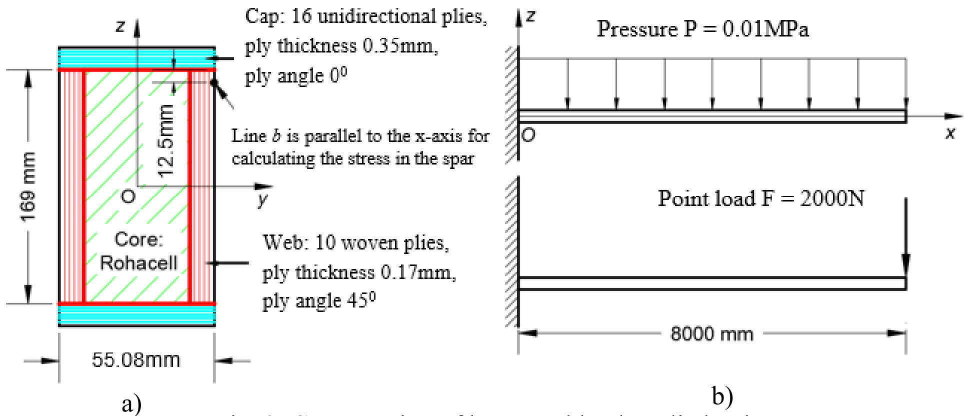

Fig. 2. Cross section of beam and load applied to it

Shear flow q is defined as the product of shear stress τ and the thickness of the section:

$$q = \tau.t \tag{27}$$

The shear flow q_s at a distance s from the edge of the web is the sum of two components: the shear flow induced by a boom B_{cap}, which carries a direct axial load $\sigma_{cap}B_{cap}$, and the shear flow induced by the normal stress distributed over the web.

$$q(s) = -\frac{S_z}{EI}\left(E_{cap}B_{cap}z_{cap} + \int_0^{h_{web}} E_{web}t_{web}.sds\right) \tag{28}$$

From shear flow expression derived above, the corresponding stresses can be calculated. The results are presented in the following section.

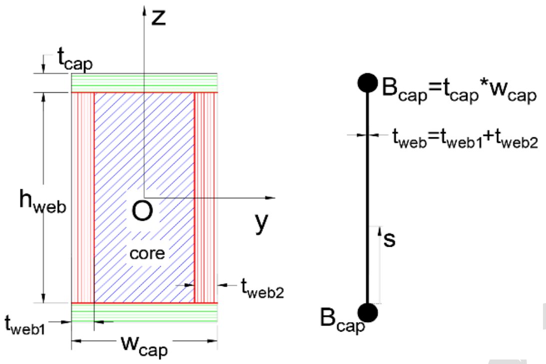

Fig. 3. Idealization of the cross-section of the beam

3. Results and Discussion

3.1 Results of Calculating Material Properties of Ply

The theory presented above is applied to two types of composite materials: AS4/3501-6 (comprising AS4 carbon fibers and 3501 epoxy resin) and IM7/977-3 (comprising IM7 carbon fibers and 977 epoxy resin). The properties of the fibers and resins are taken from reference [10], with an initial fiber misalignment angle of 2.00°. Using the theoretical framework described in Section 2.1, the results are presented in Table 2.

Table 2 shows that, overall, the calculated results agree reasonably well with the experimental data. However, discrepancies are observed in the transverse elastic moduli E_2, E_3 and the shear moduli G_{12}, G_{23}. These deviations are attributed to the parameter ξ in , which is not precisely defined and depends on both experience and the type of fiber used. A discrepancy of approximately 35%–40% is also found in the transverse compressive strength, which may be due to the incomplete consideration of fiber–matrix interactions and under transverse compression, the material may fail through various modes [10].

The woven fabric composite layer (made from AS4 carbon fibers and 3501-6 epoxy resin) can be simplified as a laminate consisting of two composite plies arranged in a $[0/90]_s$ configuration [10]. Based on this approach, the results are compared in Table 3.

Table 2. Comparison of the calculated properties of the unidirectional composite ply

Properties	AS4/3501-6		IM7/977-3	
	Present	**Exp** [10]	**Present**	**Exp** [10]
Fiber volume ratio	0.63		0.65	
Longitudinal modulus E_1 (GPa)	149,6	147.0	190	190
Transverse modulus $E_2 = E_3$ (GPa)	8.9	10.3	9.9	9.9
Shear modulus $G_{12} = G_{13}$ (GPa)	5.7	7.0	4.5	7.8
Shear modulus G_{23} (GPa)	3.5	3.7	--	--
Poisson's ratio $\nu_{12} = \nu_{13}$	0.256	0.27	0.25	0.35
Poisson's ratio ν_{23}	0.521	0.54	--	--
Longitudinal tensile strength $s_L^{(+)}$ (MPa)	2356	2280	3384	3250
Transverse tensile strength $s_T^{(-)}$ (MPa)	50.7	57	60	62
Longitudinal compressive strength $s_L^{(-)}$ (MPa)	1723	1725	1691	1590
Transverse compressive strength $s_T^{(-)}$ (MPa)	147	228	117	200
Shear strength s_{LT} (MPa)	56	76	31	75

Table 3. Comparison of the calculated properties of the woven composite ply

Properties	**Present**	**Exp** [10]	**Properties**	**Present**	**Exp** [10]
Longitudinal modulus E_1 (GPa)	78	77	Longitudinal tensile strength $s_L^{(+)}$ (MPa)	1157	963
Transverse modulus E_2 (GPa)	78	75	Transverse tensile strength $s_T^{(-)}$ (MPa)	1070	856
Transverse modulus E_3 (GPa)	11.5	13.8	Out-of-plane tensile strength $s_T^{(-)}$ (MPa)	94	60
Shear modulus G_{12} (GPa)	5.5	6.5	Longitudinal compressive strength $s_L^{(-)}$ (MPa)	1523	900
Shear modulus G_{23} (GPa)	4.5	4.1	Transverse compressive strength $s_T^{(-)}$ (MPa)	1475	900
Shear modulus G_{13} (GPa)	4.5	5.1	Out-of-plane compressive strength $s_T^{(-)}$ (MPa)	425	813
Poisson's ratio ν_{12}	0.028	0.06	Shear strength s_{LT} (MPa)	57	71
Poisson's ratio ν_{23}	0.4475	0.37	Shear strength s_{LT} (MPa)	67	65
Poisson's ratio ν_{13}	0.4475	0.50	Shear strength s_{LT} (MPa)	67	75

The results in Table 3 show that the elastic moduli and Poisson's ratios agree reasonably well with the experimental data. The tensile and shear strengths also match the experimental results fairly well, but significant discrepancies remain in the compressive strength.

3.2. Results of Stress, Displacement, and Inverse Safety Factor Calculations

The material properties obtained above are employed to compute the stress, displacement, and inverse safety factor of a beam made of AS4/3501-6 composite. The laminate stacking sequences of the composite beam components and the applied loading conditions are shown in Fig. 2. The analysis is carried out using the methodology described in Section 2.3. In addition, the composite beam is modeled in ANSYS ACP and structurally analyzed using the Static Structural module. The results obtained from both approaches are compared to verify the accuracy of the theoretical model.

The displacement of the beam under two loading conditions is compared in Fig. 4. The theoretical predictions show good agreement with the simulation results, with the maximum displacement occurring at the free end of the beam. In the case of a concentrated load, the maximum displacement from the simulation is 486 mm, compared to 460 mm from the theoretical model, corresponding to a deviation of 5.3%. For the uniformly distributed load, the maximum displacements obtained from simulation and theoretical analysis are 377 mm and 380 mm, respectively, with a deviation of only 0.8%.

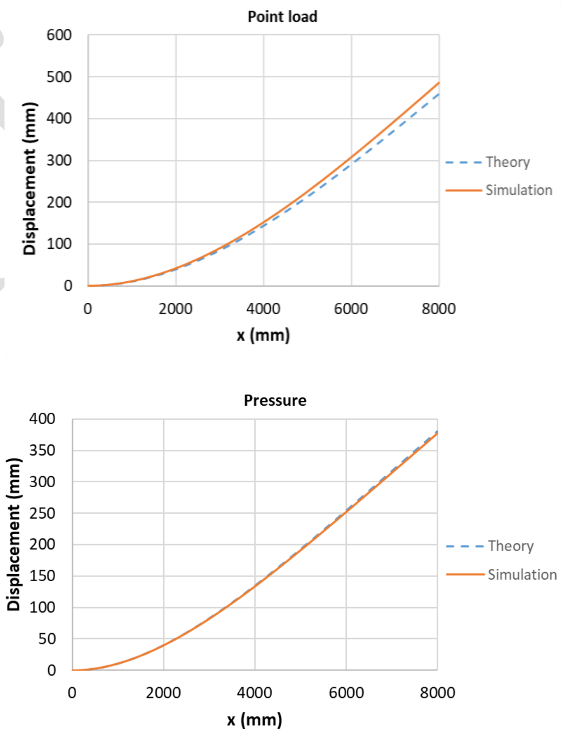

Fig. 4. Displacement along the beam under two loading conditions

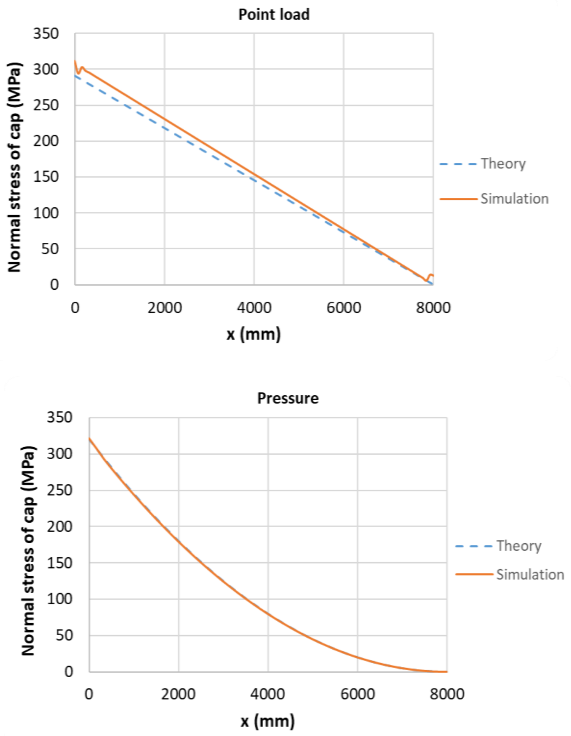

Fig. 5. Normal stress at the top ply of the cap along the beam

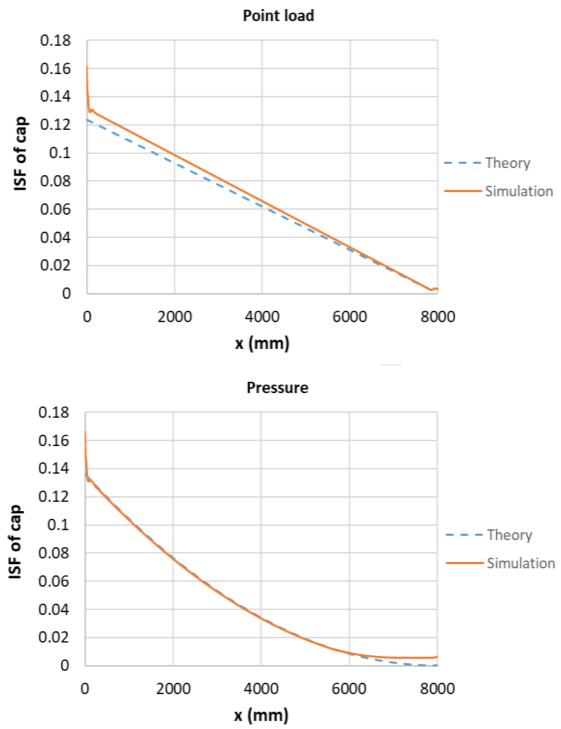

Fig. 6. ISF in the cap's top ply along the beam length

Fig. 5 compares the normal stress at the top ply of the beam cap. For both loading cases, the stress distribution along the beam predicted by the theoretical model and the simulation shows similar trends, with the maximum stress occurring at the fixed end and the minimum at the free end. Under the concentrated load, the stress varies linearly along the beam length, and the maximum stress at the fixed end differs by approximately 6.4%. In the case of a uniformly distributed load, the results from the two approaches show no noticeable difference.

The Inverse Safety Factor (ISF) is defined as the ratio of the applied load to the failure load. The ISF can be evaluated using different failure criteria. In this study, the ISF is calculated based on the Tsai-Hill failure criterion. For the cap, the top ply experiences the highest stress and is therefore used for ISF evaluation. The ISF results for the two loading conditions are presented in Fig. 6. Under the concentrated load, the ISF decreases linearly along the beam length. In the case of a uniformly distributed load, the results from the two approaches show no significant difference.

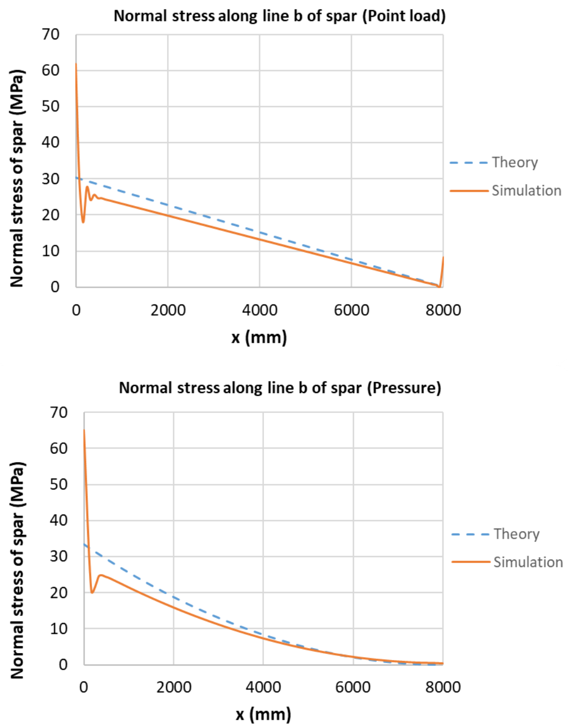

Fig. 7. Normal stress on the line b of the web

The upper edge of the beam web is typically the location of maximum stress. However, due to its direct interface and mechanical interaction with the beam cap, accurately evaluating the stress at this point is challenging. To address this, the stress components and ISF of the web are instead evaluated at location b, as marked in Fig. 2b, and the corresponding results are presented in Fig. 7. Under both loading conditions, the theoretical predictions of normal stress show generally good agreement with the simulation results, with an average deviation of about 11%, except in the vicinity of the fixed end. In this region, the simulation reveals a pronounced stress peak caused by stress concentration effects, which are not accounted for in the theoretical model. In engineering practice, such regions are often reinforced to enhance structural strength and compensate for these limitations in theoretical analysis.

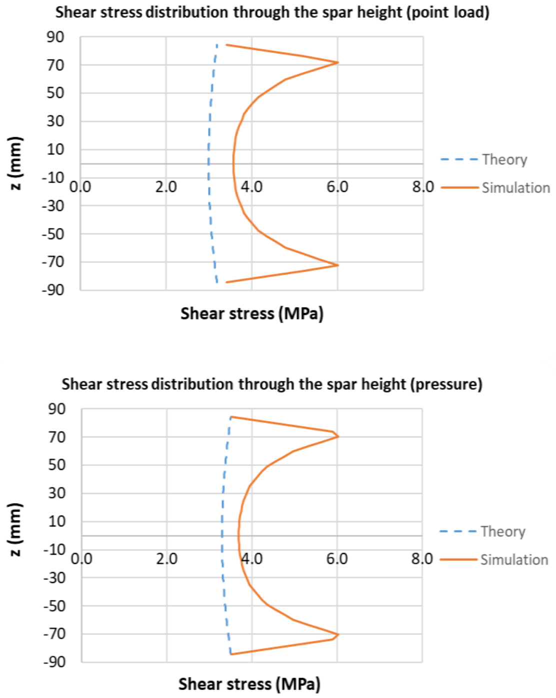

Fig. 8. The variation of shear stress in the beam web along the z-coordinate

Fig. 8 illustrates the variation of shear stress in the beam web along the z-coordinate at the cross-section located at x equal 4000 mm. It is observed that the shear stress decreases as the point approaches the neutral axis. The theoretical results for both loading cases fall within the range of 3.0–3.5 MPa, which are lower than those obtained from the simulation.

Since both the beam cap and web are thin composite laminates, plane stress conditions are assumed. The dominant stresses are normal (Fig. 7) and shear (Fig. 8), so the ISF is calculated from these components (Fig. 9). Under a concentrated load, the ISF varies linearly, with a maximum deviation of 16% near the fixed end, while for a uniformly distributed load, the deviation at the beam root is about 10%.

For the beam core, the maximum normal stresses from theory and simulation are 0.136 MPa and 0.140 MPa under a concentrated load, and 0.151 MPa and 0.131 MPa under a pressure load (theoretical value about 13% higher). All values are far below the core's tensile and compressive strengths, confirming safe stress levels in both cases.

Overall, the theoretical and simulation results agree well, with discrepancies appearing mainly at the beam ends due to stress concentrations not captured by the model. In practice, these critical regions are usually reinforced to address such limitations.

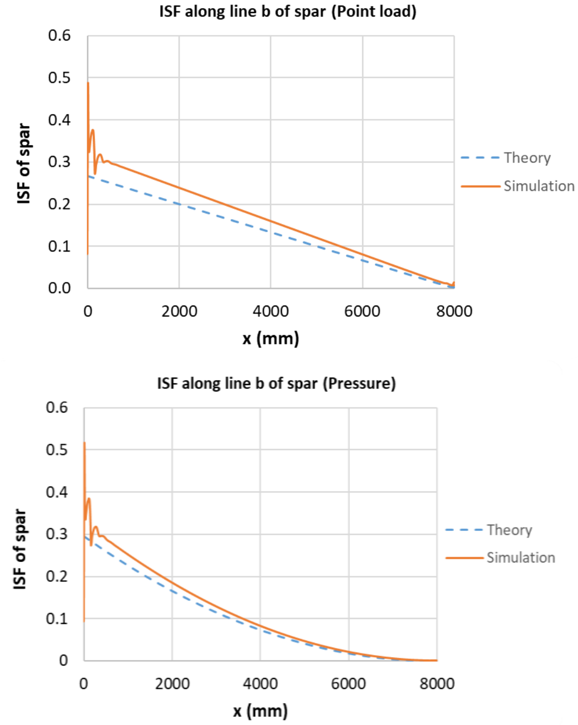

Fig. 9. ISF on the line b of the spar

4. Conclusion

This paper presents a multi-fidelity structural analysis of a composite beam, beginning with the evaluation of lamina and laminate properties - derived from micromechanics theory and CLT, respectively -and followed by beam analysis. The calculated properties agree well with experimental data. Using these properties, Euler-Bernoulli beam theory is applied to predict stress, displacement, and the ISF for a cantilever beam under concentrated and uniformly distributed loads. Theoretical results show strong consistency with simulations. The study provides a basis for efficient models to rapidly predict the mechanical response of aircraft and UAV structures in preliminary design.

References

[1] R. F. Gibson, Principles of Composite Material Mechanics, 2nd ed., Boca Raton, FL, USA: CRC Press, 2016.

[2] S. Palanisamy, K. Vijayananth, T. M. Murugesan, M. Palaniappan, and C. Santulli, The prospects of natural fiber composites: A brief review, International Journal of Lightweight Materials and Manufacture, vol. 7, iss. 4, pp. 496–506, Jul. 2024. https://doi.org/10.1016/j.ijlmm.2024.05.001

[3] JJ Caruso, CC Chamis, Assessment of simplified composite micromechanics using three-dimensional

finite-element analysis, Journal of Composites Technology and Research, vol. 8, iss. 3, pp. 77–84, Sep. 1986. https://doi.org/10.1520/CTR10326J

[4] E. J. Barbero, J. Trovillion, J. A. Mayugo, and K. K. Sikkil, Finite element modeling of plain weave fabrics from photomicrograph measurements, Composite Structures, vol. 73, no. 1, pp. 41–52, May 2007. https://doi.org/10.1016/j.compstruct.2005.01.030

[5] S. D. Müzel, E. P. Bonhin, N. M. Guimarães, and E. S. Guidi, Application of the finite element method in the analysis of composite materials: A review, Polymers, vol. 12, no. 4, Art. no. 818, Apr. 2020. https://doi.org/10.3390/polym12040818

[6] Z. Zhang and K. Friedrich, Artificial neural networks applied to polymer composites: A review, Composites Science and Technology, vol. 63, iss. 14, pp. 2029–2044, Nov. 2003. https://doi.org/10.1016/S0266-3538(03)00178-6

[7] Y. Sun, I. Hanhan, M. D. Sangid, and G. Lin, Predicting mechanical properties from microstructure images in fiber-reinforced polymers using convolutional neural networks, Journal of Composites Science, vol. 8, no. 10, Art. no. 387, Sep. 2024. https://doi.org/10.3390/jcs8100387

[8] J. C. H. Affdl and J. L. Kardos, The Halpin–Tsai equations: A review, Polymer Engineering and Science, vol. 16, no. 5, pp. 344–352, May 1976. https://doi.org/10.1002/pen.760160512

[9] M. Meng, H. R. Le, M. J. Rizvi, and S. M. Grove, 3D FEA modelling of laminated composites in bending and their failure mechanisms, Composite Structures, vol. 119, pp. 693–708, Jan. 2015. https://doi.org/10.1016/j.compstruct.2014.09.048

[10] I. M. Daniel and O. Ishai, Engineering Mechanics of Composite Materials, 2nd ed. New York, NY, USA: Oxford University Press, 2006.

[11] X. Chen, X. Sun, P. Chen, B. Wang, J. Gu, W. Wang, Y. Chai, and Y. Zhao, Rationalized improvement of Tsai–Wu failure criterion considering different failure modes of composite materials, Composite Structures, vol. 256, Jan. 2021, Art. no. 113120. https://doi.org/10.1016/j.compstruct.2020.113120

[12] T. H. G. Megson, Aircraft Structures for Engineering Students, 4th ed. Oxford, UK: Elsevier, 2022.